

Wake dynamics of external flow past a curved circular cylinder with the free stream aligned with the plane of curvature

A. MILIOU, A. DE VECCHI, S. J. SHERWIN
AND J. M. R. GRAHAM

Department of Aeronautics, Imperial College London, South Kensington Campus,
London, SW7 2BY, UK

(Received 16 October 2006 and in revised form 7 July 2007)

Three-dimensional spectral/*hp* computations have been performed to study the fundamental mechanisms of vortex shedding in the wake of curved circular cylinders at Reynolds numbers of 100 and 500. The basic shape of the body is a circular cylinder whose centreline sweeps through a quarter section of a ring and the inflow direction lies on the plane of curvature of the quarter ring: the free stream is then parallel to the geometry considered and the part of the ring that is exposed to it will be referred to as the ‘leading edge’. Different configurations were investigated with respect to the leading-edge orientation. In the case of a convex-shaped geometry, the stagnation face is the outer surface of the ring: this case exhibited fully three-dimensional wake dynamics, with the vortex shedding in the upper part of the body driving the lower end at one dominant shedding frequency for the whole cylinder span. The vortex-shedding mechanism was therefore not governed by the variation of local normal Reynolds numbers dictated by the curved shape of the leading edge. A second set of simulations were conducted with the free stream directed towards the inside of the ring, in the so-called concave-shaped geometry. No vortex shedding was detected in this configuration: it is suggested that the strong axial flow due to the body’s curvature and the subsequent production of streamwise vorticity plays a key role in suppressing the wake dynamics expected in the case of flow past a straight cylinder. The stabilizing mechanism stemming from the concave curved geometry was still found to govern the wake behaviour even when a vertical extension was added to the top of the concave ring, thereby displacing the numerical symmetry boundary condition at this point away from the top of the deformed cylinder. In this case, however, the axial flow from the deformed cylinder was drawn into the wake of vertical extension, weakening the shedding process expected from a straight cylinder at these Reynolds numbers. These considerations highlight the importance of investigating flow past curved cylinders using a full three-dimensional approach, which can properly take into account the role of axial velocity components without the limiting assumptions of a sectional analysis, as is commonly used in industrial practice. Finally, towing-tank flow visualizations were also conducted and found to be in qualitative agreement with the computational findings.

1. Introduction

A quarter segment of a ring can be considered as a generic shape for a deformed catenary riser pipe. Within the bluff-body flow community, there is an extensive amount of literature on various aspects of the flow past a straight cylinder. Although

the different flow regimes occurring at increasing Reynolds numbers for a straight cylinder have been widely studied and other aspects such as a sheared inflow and vortex-induced vibrations have also been broadly investigated, the wake behind curved or deformed cylinders have naturally received much less attention.

The initiation of vortex shedding for a straight circular cylinder is observed to occur at Reynolds numbers between 47 and 49. At low Reynolds numbers, the wake of the straight circular cylinder can remain two-dimensional with careful control of the end conditions. The two-dimensional wake then undergoes transition to three-dimensionality in two stages that manifest themselves also as discontinuities in the Strouhal–Reynolds number curve (Williamson 1988). The first discontinuity occurs at a Reynolds number of approximately 180 and has been named Mode A. It involves the deformation of the spanwise vortices in a wavy fashion and the formation of streamwise vortex loops. The second discontinuity is associated with a change in the type of three-dimensional structures in the wake, from vortex loops to finer-scale streamwise vortices. It has been labelled Mode B and comprises a gradual transfer of energy from Mode A shedding, which occurs at Reynolds numbers between 230 and 260. The character of each discontinuity is markedly different: in Mode B the flow behaviour does not exhibit a hysteresis, as found for Mode A, and the transition occurs smoothly over a larger range of Reynolds numbers. Blackburn, Marques & Lopez (2005) have studied the transition modes using Floquet stability analysis. When only one parameter is varied (i.e. the Reynolds number), three different bifurcations are possible in the passage from two-dimensional to three-dimensional flow: the long- and short-wavelength instabilities in the wake, Modes A and B respectively, are synchronous with real Floquet multipliers and represent a primary and secondary bifurcation. The third mode is a quasi-periodic state, which is not critical in this range of Reynolds numbers (up to 280 approximately), but becomes unstable at $Re \approx 377$ and gives rise either to a modulated travelling wave or to a modulated standing wave.

When considering the effect of curvature, the flow past a ring normal to the flow has previously been investigated by several researchers. Takamoto & Izumi (1981) reported on the stable arrangement of vortex rings developed in experiments behind an axisymmetric ring at low Reynolds numbers. Bearman & Takamoto (1988) investigated the wake structures developed past rings and disks in a wind tunnel where the models were suspended normal to the free stream at Reynolds numbers of the order of 10^4 . Leweke & Provansal (1995) studied the wake of high-aspect-ratio rings at low Reynolds numbers. In the Reynolds-number range between 50 and 200 they found that, depending on the initial conditions, different modes of vortex shedding could occur: with smooth initial conditions, the parallel modes dominated in this investigation. Miliou, Sherwin & Graham (2003) presented a numerical simulation of the shedding patterns past a curved cylinder (a quarter of the ring geometry) at a Reynolds number of 100. In-phase shedding along the span was detected with vortex rings shed periodically, parallel to the body, in agreement with Leweke & Provansal (1995). With the flow normal to the plane of curvature, a qualitative behaviour similar to that expected for a straight two-dimensional cylinder was observed.

A configuration where the upstream flow is parallel to the plane of curvature has, however, received comparably little attention, but is of great interest in marine hydrodynamics, especially in off-shore applications such as flexible riser pipes that deform under the effect of ocean streams and waves. In the present work, numerical investigations have been performed at Reynolds numbers of 100 and 500: although these values are several orders of magnitude lower than a realistic range ($Re \approx 10^6$ for riser pipes), they allow a better representation of the basic shedding modes which

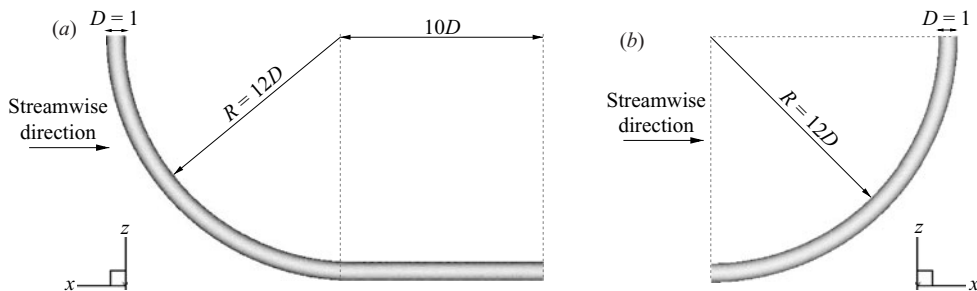


FIGURE 1. (a) Definition of convex configuration; a ten diameter horizontal extension is included; (b) definition of concave configuration.

have been investigated mainly for straight cylinders. We believe that a complete study of the fundamental features of vortex formation and shedding for curved geometries must be undertaken before considering more complex and turbulent dynamics. In addition, flow, visualization experiments have been conducted alongside the numerical simulations.

This paper is arranged as follows. Section 2 presents the problem definition and a brief overview of the computational method employed, data analysis and convergence tests. Section 3 details the results of the three-dimensional computations for the first geometrical configuration, and in §4 we discuss these findings. In §5, we present the flow past the second configuration and these results are discussed in §6. Finally, we conclude and summarize in §7.

2. Problem definition and computational techniques

2.1. Problem definition

As outlined in §1, the main component of the geometry is a circular cross-sectioned cylinder whose centreline is a quarter of a ring (torus). (Strictly speaking it should be a pipe, but we have chosen to use cylinder because of the convention in the literature of external flow past circular cylinders and internal flow within circular pipes.) The non-dimensional radius of curvature is defined as the ratio of the radius, R , of the curved axis of the deformed cylinder to the cross-section diameter, D , of the cylinder. In all the numerical investigations presented in this paper, the curved circular cylinder has a non-dimensional radius of curvature, R/D , of 12.5, as figure 1 depicts.

In studies of a full ring the aspect ratio, defined as the ratio between the external perimeter of the ring and the cylinder cross-section diameter, has been used to parameterize the geometry. If we were to calculate an analogous parameter for the quarter of a ring studied here, the aspect ratio would be 81.7. From Leweke & Provansal (1995) and Bearman & Takamoto (1988), when the aspect ratio is above 20, the wake patterns of flow perpendicular to the plane of the ring have been observed to approximate those of a straight cylinder. The computations presented in this paper involve a uniform incident velocity profile and two types of bodies (figure 1). We define the Reynolds number as $Re = U_\infty D / \nu$, where U_∞ is the free-stream velocity. The ‘convex bend’ configuration is a quarter ring with a horizontal straight cylinder of ten diameters added onto the end of the ring; a uniform flow parallel to the plane of curvature has been applied outside the bend (figure 1a). The second body, referred to as the ‘concave bend’, involves only the quarter ring part of the first body rotated about the z -axis by $\pi/2$; a third configuration has been obtained by adding a vertical

extension, 6 diameters long, on the top of the concave geometry. In both cases, a uniform flow parallel to the plane of curvature has been applied on the inside of the bend.

2.2. Navier–Stokes solver

The three-dimensional computations have been performed using a spectral/*hp* element Navier–Stokes solver developed by Sherwin & Karniadakis (1996) and Karniadakis & Sherwin (1999). Spectral/*hp* element methods combine attributes of both finite-element and spectral methods: one can increase simultaneously the number of elements in the domain, *h*-refinement, and the order of the polynomial expansions within the element, which is referred to as *p*-refinement. The temporal discretization of the Navier–Stokes equations is achieved by a stiffly stable splitting scheme (Karniadakis, Israeli & Orszag 1991). In order to determine the fields at t_{n+1} , the velocity and pressure at time t_n are calculated in three substeps over a time step Δt . The nonlinear terms are treated explicitly, while a Poisson equation for pressure is obtained by enforcing the incompressibility constraint on an intermediate velocity field. Finally, the linear terms are treated implicitly and the final velocity field is obtained through the solution of a Helmholtz equation. Therefore, in a full time step, a Helmholtz equation is solved for each of the velocity components and a Poisson equation is solved for pressure.

2.3. Mesh generation

The mesh generation for all the computational investigations has been accomplished by *Felisa* (Peiró, Peraire & Morgan 1994). A variant of the advancing front method (Peraire, Peiró & Morgan 1993) is employed for the triangulation of the domain surfaces and the generation of the three-dimensional tetrahedral mesh. For the generation of a boundary-layer mesh near the cylinder wall regions, a modified advancing layers method (Peiró & Sayma 1995) has also been employed whereby the nodes of the mesh in the neighbourhood of the solid boundaries are generated along lines that are approximately normal to the surface. At the surface, spectral/*hp* elements are allowed to deform to model consistently the curved surface, as described in Sherwin & Peiró (2002). As indicated in figure 1, the cylinder was aligned to the (x, z) -plane with the free-stream direction parallel to the x -coordinate. Taking the origin as the centre of rotation of the ring, the convex geometry computational domain spanned the region $-10D \leq x \leq 18D$, $-5D \leq y \leq 5D$, $-18D \leq z \leq 0$, whilst the concave geometry computational domain spanned the region $0 \leq x \leq 28D$, $-8D \leq y \leq 8D$, $-21D \leq z \leq 0$. In the convex cylinder case, the mesh was comprised of 10 250 elements, out of which 1184 were prismatic surface elements, whereas in the concave configuration the mesh consisted of 14 847 elements, out of which 1 574 were prisms. In this second case, when the computation is performed using a sixth-order polynomial expansion, the mesh accounts for 1 423 436 local degrees of freedom per variable, whereas 2 827 515 local degrees of freedom per variable are applied when an eighth-order polynomial expansion is adopted.

2.4. Numerical boundary conditions

2.4.1. Convex configuration

(i) Symmetry boundary conditions are assigned to the top boundary of the computational domain when oriented as in figure 1 (i.e. $w = 0$, $du/dn \equiv du/dz = 0$ and $dv/dn \equiv dv/dz = 0$).

	$P = 6$	$P = 8$		$P = 4$	$P = 6$	$P = 8$
C_{Fxmean}	1.2214	1.2209	C_{Fxmean}	1.0758	1.0747	1.0745
C_{Fymean}	0.0001	0.0	C_{Fymean}	0.0009	-0.0001	-0.0001
C_{Fzmean}	0.3289	0.3286	C_{Fzmean}	-0.4211	-0.4200	-0.4200

TABLE 1. Mean values for the integrated force coefficients as a function of polynomial order P for the flow past the convex configuration (left) and the concave configuration (right) at $Re = 100$.

(ii) At the outflow a fully developed zero stress condition was imposed, i.e. $du/dn = 0$, $dv/dn = 0$, $dw/dn = 0$ and $p = 0$. The length of the horizontal extension has been chosen in order to allow the wake to evolve and reach a stable state.

(iii) The free-stream velocity was imposed along all other boundaries, consisting in three Dirichlet boundary conditions for each of the velocity components and a Neumann boundary condition for the pressure.

2.4.2. Convex configuration and concave configuration with vertical extension

(i) In these cases as well, the top computational plane, which includes an intersection with the body, has been modelled using a symmetry boundary condition.

(ii) The outflow corresponds to a fully developed zero stress condition.

(iii) A velocity inlet boundary condition $U = [1, 0, 0]$ has been imposed on all the other computational planes, with the exception of the inflow where the cylinder intersects the boundary. Here the following no-slip conforming boundary condition was applied:

$$\frac{u(x, y, z)}{U_\infty} = 1 - \exp(-50(\sqrt{x^2 + y^2 + (z + 12.5)^2} - 0.5)), \quad \frac{v(y, z)}{U_\infty} = \frac{w(y, z)}{U_\infty} = 0,$$

where the exponential term has been added to the inflow to achieve exponential decay of the velocity inside the boundary layer. Away from the body, the free-stream velocity is $U_\infty = 1$.

2.5. Data analysis

In the following analysis, we consider the integrated unsteady forces acting on the cylinder. Further insight can be gained from determining the variation of these forces along the span: the lift coefficients on each two-dimensional circular section are therefore presented, allowing a better understanding of the different contribution of the three-dimensional integrated forces in each section of the cylinder. Finally, in order to investigate the wake topology developed in the flow simulated, the Jeong & Hussain (1995) λ_2 method was employed for capturing and visualizing the vortical structures. This criterion stems from the pressure minimum in the absence of unsteady or viscous contributions and dictates that in order to locate a vortex core, the second largest eigenvalue, λ_2 , of $\mathbf{S}^2 + \mathbf{\Omega}^2$ must be negative.

2.6. Convergence test

In all the simulations, the order of the polynomial expansion has been uniformly increased from 2 to 4 and then to 6 (and further to 8 in some of the computational cases). Most of the numerical results stem from computations initially performed using first-order time integration to establish the flow features, and then adopting a second-order time integration scheme. For the convex configuration at $Re = 100$, the mean values of the integrated forces computed are shown in table 1 on the left-hand side. Figure 2 illustrates the integrated force coefficients in the three Cartesian

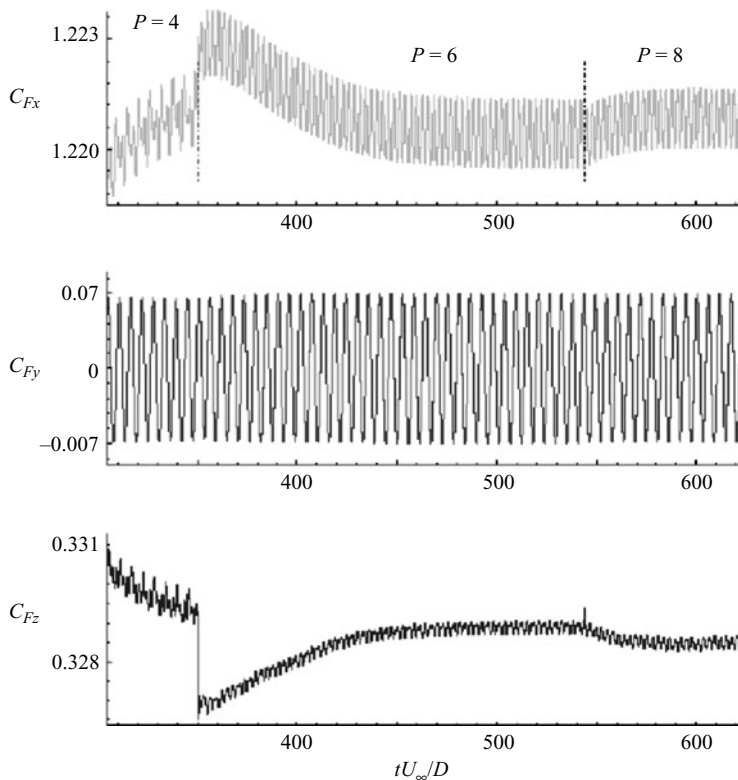


FIGURE 2. Snapshot in time for the integrated force coefficients from $t|U_\infty|/D = 305$ to $t|U_\infty|/D = 625$, part of $P = 4$ to $P = 8$. Convex configuration configuration at $Re = 100$.

directions for the same case: the transition from $P = 4$ to $P = 6$ is observed at $t|U_\infty|/D \approx 350$ and the change from order 6 to order 8 at $t|U_\infty|/D = 543$. The values of the time averaged force coefficients for $P = 6$ and $P = 8$ are in good agreement, with a maximum discrepancy of 0.03%. The simulations conducted with first- and second-order time integration were in agreement to the order of 10^{-3} . In both cases, force convergence has been achieved. Similarly, table 1 (right-hand side) shows the convergence of mean force coefficients for the concave ring at $Re = 100$: a reduction of merely 0.1% in the magnitude of C_{Fx} is observed when the polynomial order is increased from 4 to 6 and a reduction of 0.02% occurs between $P = 6$ and $P = 8$.

2.7. Sectional approximation of the flow

A common approach to modelling the hydrodynamics of the flow past a deformed cylinder in industrial practice is to use a sectional analysis based on strip theory. The flow is typically computed in two-dimensional planes that are placed at intervals along the span of the cylinder and are perpendicular to its axis. In the case of curved geometries, the onset flow is decomposed into components normal and perpendicular to the cylinder axis. Following the ‘independence principle’, only the normal component of the inflow velocity is considered to be responsible for the fluid dynamics forces generated on the body: the tangential component is typically neglected and hence the production of axial flow is ignored by this approach. If θ denotes the angle between each section plane and the free-stream flow vector, the normal component is

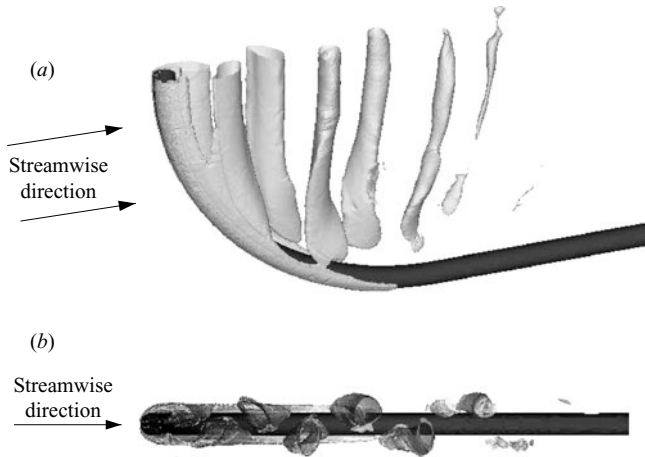


FIGURE 3. Vortex cores in the wake of the convex configuration at $Re = 100$, $\lambda_2 = -0.1$: (a) three-dimensional view extracted at a minimum of the integrated C_{Fy} , $tU_\infty/D \approx 524$, (b) view from the top.

obtained as $U_\infty \cos \theta$, whereas the axial component is equal to $U_\infty \sin \theta$. A sectional two-dimensional argument will therefore consider only the normal direction, $U_\infty \cos \theta$, at each section. These simulations are typically many orders of magnitude faster than fully three-dimensional computations: strip-theory-based codes have been used in the past to simulate more realistic Reynolds numbers for riser pipe applications (see Willden & Graham 2004; Meneghini *et al.* 2004), but the validity of their use for non-straight cylinders (where the normal velocity component along the span is not constant and the formation of axial flow significant) is still open to question and will be further discussed.

3. Results: convex configuration

3.1. $Re = 100$

Figure 3 shows a three-dimensional view of the wake topology obtained using the Jeong & Hussain (1995) criterion to compute isosurfaces at a λ_2 value of -0.1 . Figure 3(b) depicts a projection of the vortex cores onto the (x, y) -plane, i.e. viewed from the top, showing the antisymmetric wake with a staggered array of vortices. It can be seen that the vortex cores are straight close to the body with their axes normal to the free stream, but start to distort further downstream.

To understand the wake dynamics better, the variation of the horizontal transverse sectional force coefficient, C_{Fy} , has been evaluated within slices normal to the cylinder axis at different spanwise locations: the results are presented in figure 4 together with an enlarged view of the integrated force coefficients. We recall that the x -direction is the direction of the drag and the y - and z -directions represent the horizontal and vertical component of the transverse force, respectively. With s denoting the arclength measured from the upper plane, the top of the cylinder is at $s/D = 0$ whereas the vertical slice at the end of the quarter ring corresponds to a non-dimensional arclength of $s/D = 19.6$. Figures 4(a) and 4(b) show, respectively, the strong alternating vortex shedding pattern at the top of the curved cylinder and the corresponding periodic

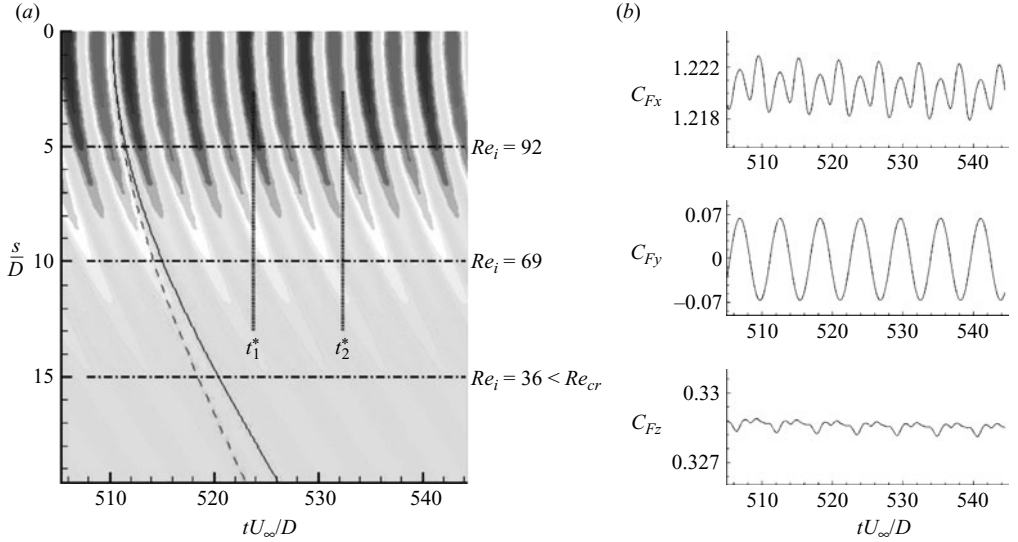


FIGURE 4. (a) Variation of sectional C_{Fy} along the length of the quarter ring part of the convex configuration, $Re = 100$. The isocontours range from -0.17 to $+0.17$. (b) Snapshot in time for the integrated force coefficients computed at $P = 8$.

oscillations of the transverse force in the y -direction: this is consistent with the vortex cores displacement in figure 3.

The observation that the main vortices are straight, similar to the in-phase shedding observed past a straight cylinder, but the sectional forces plot, (figure 4a) does not remain constant in sign along the span at a fixed time level may appear inconsistent at first. At $t_1^* \approx 524$ in figure 4(a), we observe a decrease in the magnitude of the forces as s/D increases and finally a change in the sign: this can be explained by considering the effect of the body curvature. In fact, figure 3 shows clearly that the distance between cores and cylinder decreases along the span, leading to a gradual phase change. Consequently, at different spanwise sections, the influence of the developing shear layers on the body is different and the sign of the forces changes accordingly. The dashed line in figure 4(a) represents a model for the phase variation of the sectional force along the quarter ring based on the free-stream velocity $U_C = U_\infty (=1)$, whereas the continuous line was evaluated based on the convective velocity of the vortices when $U_C = 0.8$. The relation between the body curvature and the phase variation is given by

$$\frac{tU_C}{D} = \frac{(R + D/2)(1 - \cos(s/R))}{D}. \quad (3.1)$$

This point will be discussed further in §4.

Figure 5(a) depicts the time-averaged variation of pressure along the stagnation line as well as the base pressure. To highlight the three-dimensionality of this type of flow, the variation of the \bar{u} and \bar{w} velocity components (Cartesian axes), extracted 0.3 diameters upstream in the radial direction of the curved cylinder, is shown in figure 5(b). As time-averaged pressure decreases along the stagnation line, the magnitude of the w velocity component increases along the span and reaches a maximum of 30% of the free-stream magnitude at a non-dimensional arclength of $s/D = 10$, which corresponds to a section inclined at 45.8° to the horizontal.

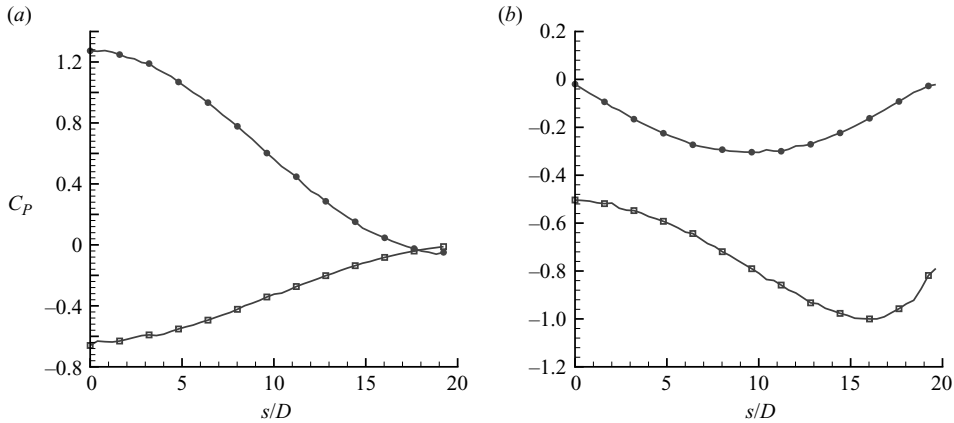


FIGURE 5. Variation of time-averaged pressure and velocity along the span of the convex configuration, $Re = 100$. (a) \bullet , Base pressure and \blacksquare , stagnation pressure, (b) \blacksquare , \bar{u} and \bullet , \bar{w} velocity components extracted 0.3 diameters upstream of the curved cylinder.

3.1.1. Experimental flow visualization

Experimental work was also conducted to compare the computational results with the flow visualizations. A model curved cylinder with the same aspect ratio as in the computational cases was towed in a water tank (Owen 2001) at an effective Reynolds number equal to that of the computations. The flow-visualization technique employed was laser-induced fluorescence. Coloured dye was adhered on the stagnation line of the curved cylinder in two slots symmetrically offset slightly from the centre. The red and green colours in the towing-tank flow-visualization images are attributed to sulfuro rhodamine and sodium fluorescein dye, respectively (Lear 2003). A Class IV laser was used to illuminate the dye diffusing from the stagnation line of the curved cylinder and the wake patterns formed.

The flow visualization obtained for this configuration is shown in figure 6. Note that, as the camera in the experiments was positioned lower than the water free surface, a reflection is introduced: the picture therefore includes the mirror image of the flow visualization in the water surface. The slight bowing of the vortices towards the top cylinder end in experiments where a straight circular cylinder is towed through a water surface has been observed previously (Slaouti & Gerrard 1981) and is due to the free surface: this is not present in the numerical results, as the upper boundary was modelled as a symmetry plane.

3.2. $Re = 500$

The flow past the convex configuration was also computed at a higher Reynolds number of 500. At this Reynolds number, a straight cylinder would exhibit three-dimensional instabilities in the wake: therefore, this study allows us to consider the role of three-dimensional wake instabilities on a curved cylinder. This computation was restarted from the §3.1 simulation at a Reynolds number of 100.

The variation of sectional C_{F_y} computed at sections normal to the cylinder axis for the convex configuration at $Re = 500$ is depicted in figure 7(a). A comparison with figure 4 at $Re = 100$ shows that the magnitude of sectional C_{F_y} does not decrease uniformly along the span; moreover, the forces persist further down the pipe, although a fundamental single period is not present in this case. As in the previous case, the

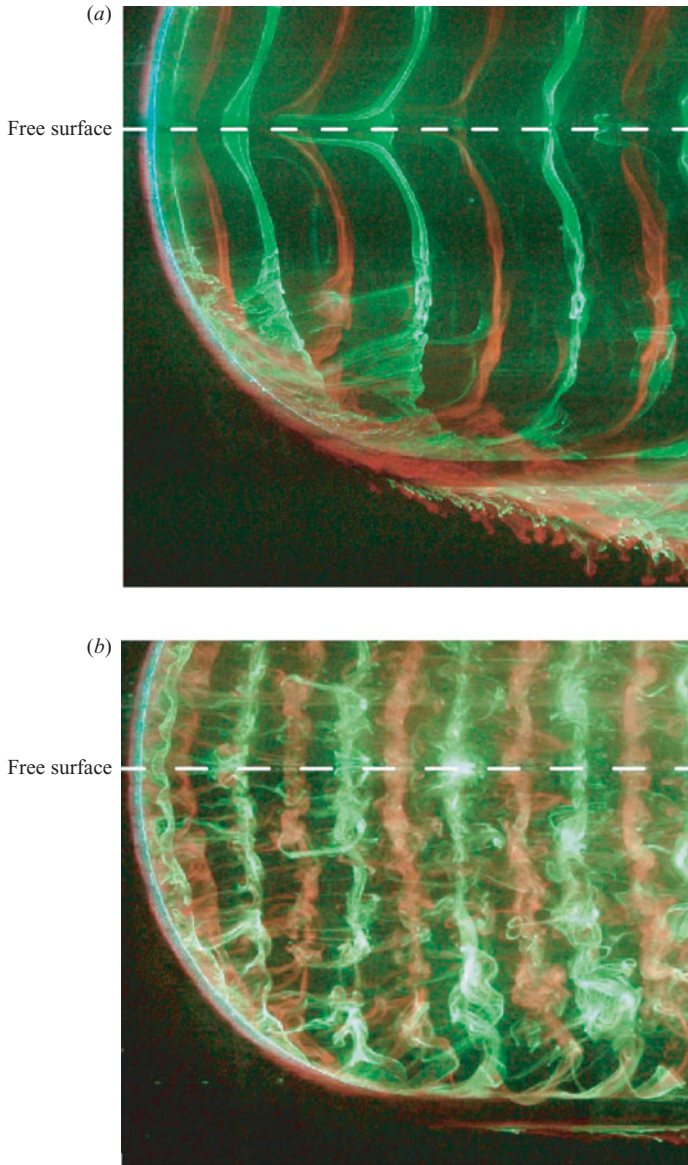


FIGURE 6. Towing-tank flow visualization: (a) convex configuration, $Re = 100$, (b) convex configuration, $Re = 500$.

phase line based on the free-stream velocity (see (3.1)) is superimposed on the sectional forces within this figure.

Figure 7(b) shows an enlarged section of the integrated force coefficients in the x -, y -, and z -directions for part of the simulation computed using sixth-polynomial order. Figure 8(a) shows the wake topology in a three-dimensional perspective, whereas figure 8(b) shows the same data viewed from the top. Both images highlight the transitional nature of the wake and the presence of small streamwise vortical structures. The region where the vortices curl above the horizontal part of the cylinder becomes more energetic owing to the increased Reynolds number. The experimental

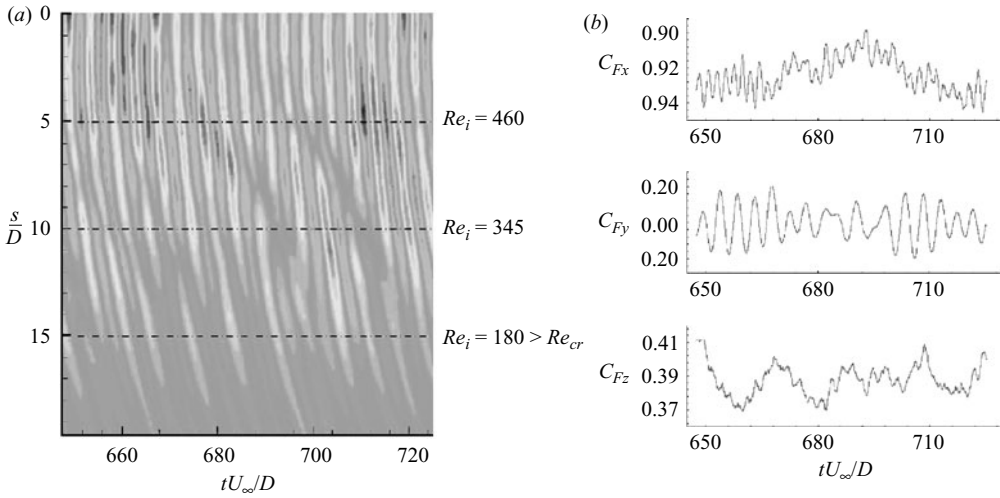


FIGURE 7. (a) Sectional C_{Fy} variation along the length of the quarter ring part of the convex configuration, $Re = 500$; the isocontours range from -0.44 to $+0.44$. (b) A detailed section of the integrated force coefficients computed at sixth-polynomial order.

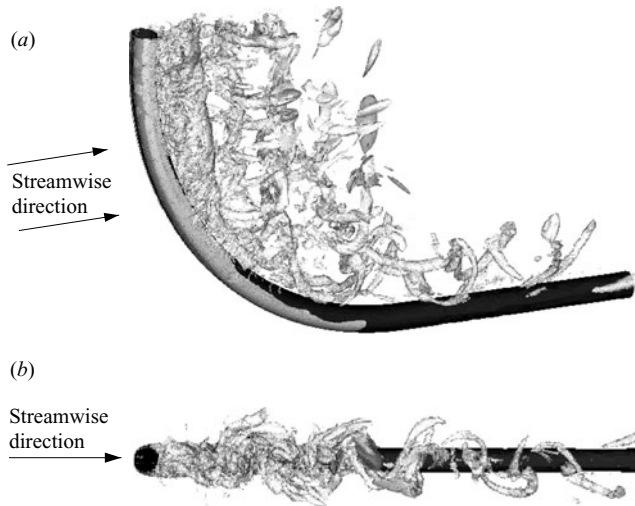


FIGURE 8. Vortex cores in the wake of the convex configuration at $Re = 500$, $\lambda_2 = -0.8$, $tU_\infty/D \approx 652$: (a) three-dimensional view, (b) view from the top.

flow visualization for this case is in good qualitative agreement with the wake topology extracted from the three-dimensional computation. The gross features of the flow with streamwise vorticity connecting the spanwise rollers can be seen in figure 6(b).

The variation of time-averaged pressure on the stagnation line and the base pressure for the convex configuration at $Re = 500$ are shown in figure 9(a), whereas figure 9(b) depicts the variation of the time-averaged streamwise (\bar{u}) and vertical spanwise (\bar{w}) velocity components extracted 0.3 diameters upstream in the radial direction of the curved cylinder. In both figures, the data is averaged over a non-dimensional time interval $tU_\infty/D = 10$. As pressure decreases along the stagnation line, the magnitude of the w velocity component increases along the span and reaches a maximum of

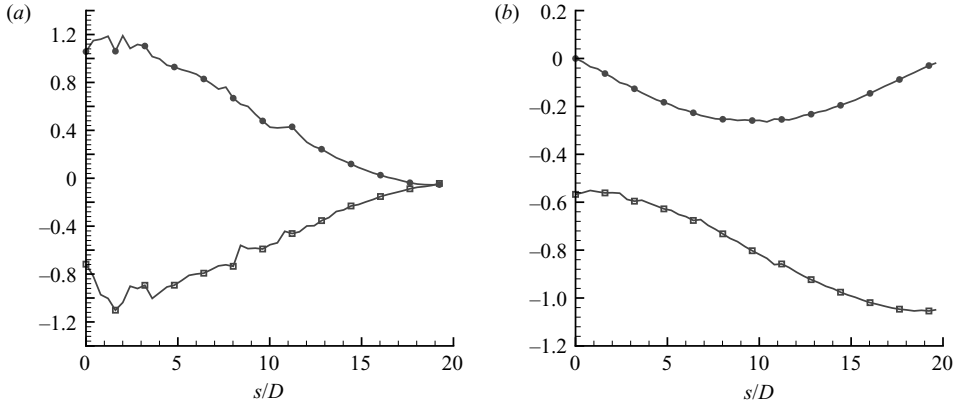


FIGURE 9. Variation of time-averaged pressure and velocity along the span of the convex configuration, $Re = 500$: (a) \bullet , base pressure and \blacksquare , stagnation pressure, (b) \blacksquare , \bar{u} and \bullet , \bar{w} velocity components extracted 0.3 diameters upstream of the curved cylinder.

approximately 26% of the free stream at a non-dimensional arclength of $s/D = 11$, which corresponds to a section inclined at 50.4° to the horizontal. This displaced location of the peak velocity as compared to the $Re = 100$ case is obviously a consequence of the increased Reynolds number and likely to be related to the increased importance of inertial over viscous effects.

4. Discussion: convex configuration

4.1. Sectional approach validity

Motivated by the reasonably common modelling practice of analysing the flow past deformed bodies using a two-dimensional sectional argument, we can consider what physical properties seem to correspond to this assumption. We recall that the sectional approximation of the flow, as introduced in §2.7, would consider the flow to be approximated by a two-dimensional slice normal to the cylinder centreline with a local onset velocity taken as the free-stream velocity component projected into this plane. Therefore, under this assumption there is an effective reduction in the local normal Reynolds number along the span as the angle of the cylinder to the incident flow changes along its length. If the flow within the sectional plane were truly two-dimensional, there will be a point at which the normal flow Reynolds number falls below the critical value for vortex shedding. Consequently, vortices will not be expected to be shed. In figure 4, a non-dimensional arclength of $s/D = 5$ corresponds to a section inclined at approximately 23° to the horizontal and a local Reynolds number, $Re_l = Re \cos \theta$, of approximately 92. Following this logic, a non-dimensional arclength of $s/D = 10$ corresponds to a section inclined about 69° to the horizontal and would have a local Reynolds numbers of 36, which is below the threshold for the onset of vortex shedding for a circular straight cylinder ($Re_l = 47 - 49$). Indeed, for this study, the vortex shedding has almost disappeared. Similarly, at $Re = 500$ the local Reynolds number in every section between $0 \leq s/D \leq 15$ is higher than this critical value and the contour levels in figure 7 depict that shedding is present.

Therefore, up to this point, the sectional approximation would seem to hold. However, from a two-dimensional sectional perspective, we would also expect to see a variation of the Strouhal number in every section along the span of the convex

configuration as the local normal Reynolds number changes. Flows past straight cylinders with varying Strouhal numbers tend to arrange themselves into cellular type patterns where different sections select discrete shedding frequencies (Gaster 1969; Gerich & Eckelmann 1982; Williamson 1989). However, the results of this study indicate that the flow past this type of curved cylinder do not behave in this manner since Strouhal frequency is constant in every spanwise section. Since the sectional Reynolds number decreases along the span as the normal velocity component decreases, this implies that St decreases continuously with sectional Re . In fact, we observe that the upper cylinder shedding drives the shedding from the lower end without frequency variation occurring along the span. As a result, there is only one dominant frequency in the C_{Fy} direction (at least for the $Re = 100$ case). This highlights one of the possible shortcomings of sectional computations for three-dimensional geometry; on the other hand, a fully three-dimensional approach involves a very high computational cost, resulting in severe restrictions on its application to realistic Reynolds-number ranges.

4.2. Phase variation and wake topology at $Re = 100$ and $Re = 500$

At $Re = 100$, the vortex cores are straight close to the body, which would tend to imply, at first impression, that shedding is in-phase. However, since the geometry is curved and cylinder and forces are usually considered in the frame of reference of the body, the distance between the cylinder and any single straight vortex core varies along the span. Therefore, when considering sectional forces as shown in figure 4(a) and 7(a), there is a spanwise variation of the shedding from the cylinder and a phase change in the sectional forces. This phase change can easily be modelled by (3.1) with an assumption about the mean vortex convection speed.

At $Re = 500$, the vortex cores are more energetic than at lower Reynolds number, especially close to the horizontal extension, as indicated by the longer downstream existence of the coherent structures (figure 8). However, we also note in this figure that the wake topology exhibits a combination of vertical rollers and braids, which are commonly associated with Mode A and B transitions in flow past a straight cylinder (Williamson 1988; Barkley, Tuckerman & Golubitsky 2000). At this higher Reynolds number, we would expect to see more evidence of the shorter wavelength Mode B structure which is reasonably evident in both figures 8 and 6(b). Finally, we note also that in this case, the phase line based on the free-stream velocity matches the sectional forces isocontours more closely than in the plot at $Re = 100$, suggesting that the increased Reynolds number leads to a more in-phase shedding.

4.3. Axial flow generation

Moving away from the idea of sectionally analysing the flow, we observe that there is a significant motion of flow along the length of the curved cylinder (see figures 5 and 9). The curved nature of the stagnation face in the convex configuration has the effect of deflecting a significant amount of the approaching flow (approximately one third of the total flow rate) towards the bottom of the cylinder. The increasingly dominant axial flow component parallel to the curved cylinder, combined with the reduction in the normal flow component, changes the body from ‘bluff’ to effectively ‘slender’: at $s/D = 13$, which corresponds to a section inclined at 60° to the horizontal, the axial flow reaches a maximum of 81% of the free-stream velocity at $Re = 100$, while the normal velocity component is approximately $0.1U_\infty$. Therefore, along the lower part of the curved cylinder, as it becomes aligned with the free stream, we observe that vortex shedding in the near wake becomes less vigorous, although synchronous with the upper part of the body.

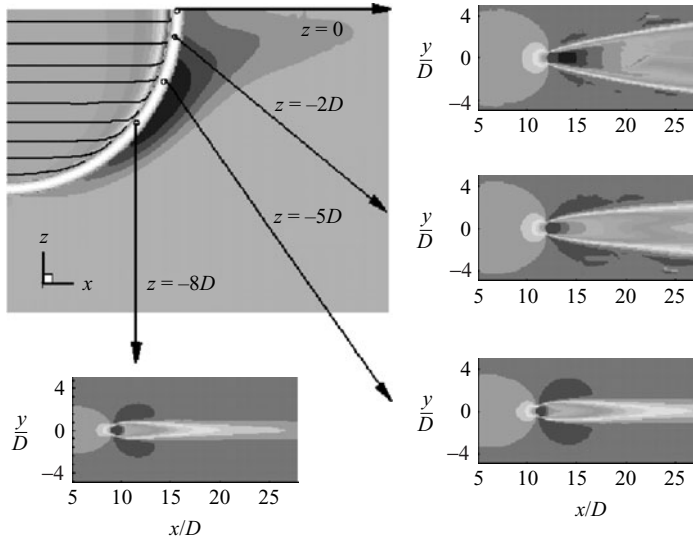


FIGURE 10. Centreplane streamlines ($y=0$) overlaid on pressure contours for the flow past the concave configuration at $Re = 100$. The insets show u velocity contours at horizontal slices located at the top plane, and 2, 5 and 8 diameters vertically below.

5. Results: concave configuration

5.1. Basic geometry, $Re = 100$

Contrary to the flow past the convex geometry, this configuration does not exhibit vortex-shedding features and therefore forces appear to be steady in all directions. Owing to the suppression of vortex shedding and hence the removal of energy transport away from the body, it is not surprising that the magnitude of the drag force is smaller by 12% compared to the convex configuration (comparing both at $P = 8$). The ratio of pressure and friction drag, C_{Dprms}/C_{Dfrms} , is equal to 1.24: this value is similar to that obtained for the convex case at $Re = 100$ where $C_{Dprms}/C_{Dfrms} \approx 1.28$.

Centreplane streamlines upstream of the curved cylinder superimposed on pressure contours are shown in figure 10. Similar to the convex configuration, the streamlines indicate motion along the length of the cylinder, but this is now directed towards the top computational plane, consistent with the shape of the stagnation face for this configuration. Figure 10 also depicts the streamwise u velocity contours in the vicinity of the cylinder at four different horizontal planes located in the top surface and at 2, 5 and 8 diameters vertically below. These velocity contours show symmetric wakes consistent with the force plots. Moreover, a variation in the wake width along the span can be observed, with the top slice exhibiting the widest wake and the bottom one the narrowest. Figure 11 illustrates the three-dimensional wake topology: the λ_2 isocontours highlight the absence of interaction between the shear layers.

Similar to our analysis of the convex configuration, figure 12 depicts the variation of pressure and velocity components along the span of the concave configuration. The magnitude of the \bar{w} velocity component increases, and reaches a maximum of approximately 22% of the free-stream value at a section inclined at 45.8° to the horizontal. The magnitude of the \bar{w} velocity component reaches a maximum along the span at exactly the same location, 45.8° to the horizontal, in both the convex and concave configurations, suggesting that this depends primarily on the geometry.



FIGURE 11. Wake topology for the flow past the concave configuration at $Re = 100$, $\lambda_2 = -0.01$.

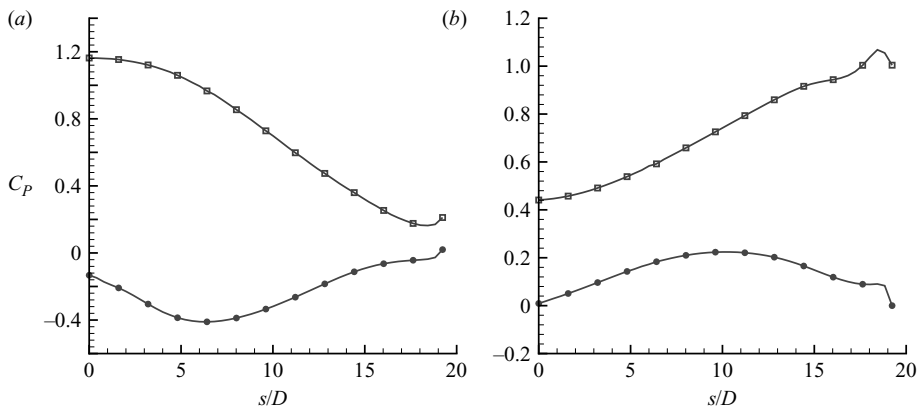


FIGURE 12. Variation of time-averaged pressure and velocity along the span of the concave configuration, $Re = 100$: (a) \bullet , base pressure and \blacksquare , stagnation pressure, (b) \blacksquare , \bar{u} and \bullet , \bar{w} velocity components extracted 0.3 diameters upstream of the curved cylinder.

Finally, we note that additional computations were performed to investigate the effect of domain size (blockage) on the present results. The domain size in the horizontal y -direction was varied until a blockage of 3.9% was achieved following Maskell's theory (see Maskell 1963) and the results were found to be free from the effects of blockage.

5.2. Influence of the symmetry plane, $Re = 100$

The nature of this geometry is to drive the flow towards the top of the computational domain where we have imposed a potentially artificial symmetry boundary condition. To investigate the role of this boundary condition, a vertical extension, 6 diameters long, was added to the concave configuration (figure 13). The 6-diameter extension represents a substantial addition of almost 50% of the height of the concave configuration.

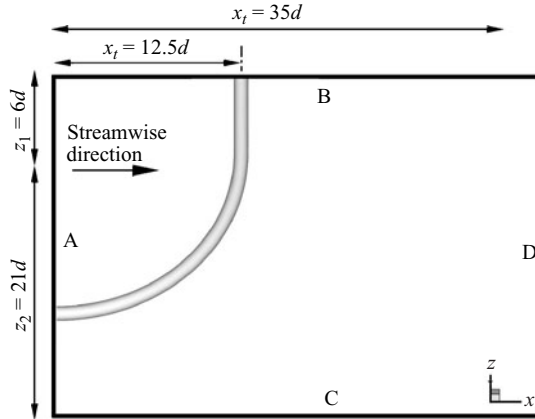


FIGURE 13. Computational boundaries (not to scale) in a plane including the free-stream vector for the concave configuration (plotted to scale) with a straight cylinder addition of 6 diameters.

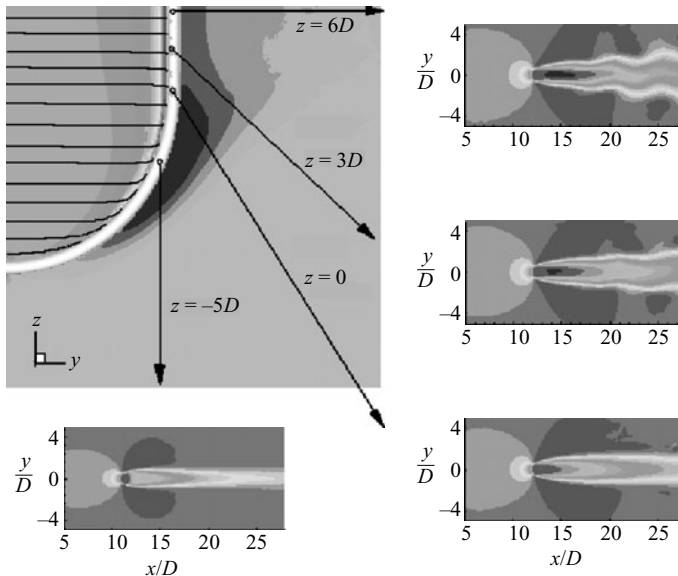


FIGURE 14. Centreplane streamlines ($y = 0$) overlaid on pressure contours for the flow past the concave configuration with a vertical extension of 6 diameters, $Re = 100$, $tU_\infty/d = 414$ (C_{Fy} maximum). The insets depict u velocity contours at four horizontal slices along the span.

Figure 13 depicts the computational domain size in the plane including the cylinder axis and the free-stream vector for this configuration. The flow is in the positive x -direction, from left to right on the page. The same boundary conditions on the corresponding planes were assigned as in the concave configuration without vertical extension: boundary D corresponds to the outflow plane and boundaries A and C correspond to free-stream boundaries where the velocity condition $U_\infty = [1, 0, 0]$ was imposed away from the body.

Figure 14 displays centreplane streamlines upstream of the geometry superimposed on pressure contours and u velocity contours at horizontal planes analogous to

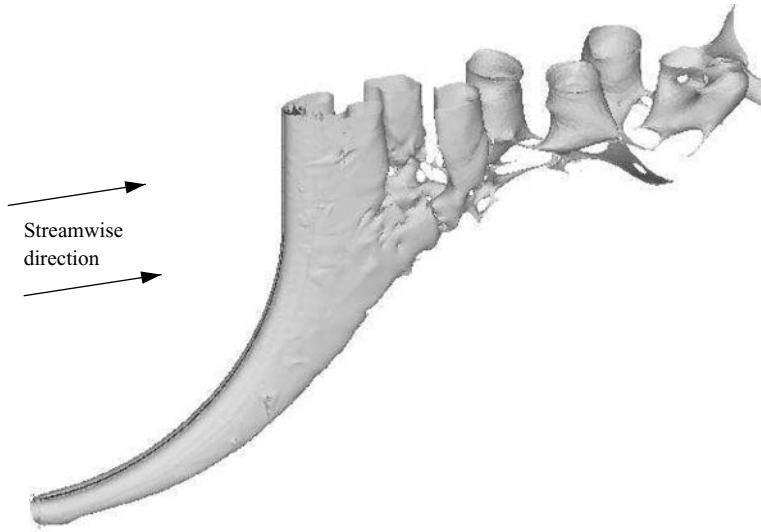


FIGURE 15. Wake topology for the concave configuration with a 6-diameter vertical extension at $Re = 100$, $\lambda_2 = -0.01$ extracted at a C_{Fy} maximum, $tU_\infty/D = 414$.

figure 10. The streamlines show that in the region of the curved cylinder, the motion is still towards the top boundary. The u velocity contours now demonstrate unsteadiness at the top plane, which is located at the end of the 6-diameter straight cylinder extension, and at the midspan of the straight cylinder addition. However at $z = 0$, which represents the end of the curved cylinder part, the wake is narrow and symmetric. This suggests that the alternating vortex shedding might resume if the straight cylinder extension were made somewhat longer than the 6-diameters tested.

Figure 15 illustrates the wake topology for this case. The variation of sectional C_{Fy} and the integrated force coefficients are shown in figures 16(a) and 16(b), respectively. Note that the range in the contour levels plotted is now between -0.025 and 0.025 , slightly higher than the range for the concave configuration, but still an order of magnitude smaller than that for the convex configuration: the fluctuations in the integrated C_{Fy} can hence be attributed to the unsteady features in the 6-diameter straight cylinder addition. The forces in the y -direction exhibit periodic oscillations whose magnitude, however, is much smaller than that for the flow past the convex configuration at the same Reynolds number. The Strouhal frequency corresponding to the periodic fluctuations in C_{Fy} is found to be 0.1142 when $P = 4$ and 0.1123 when $P = 6$. This frequency is smaller than the Strouhal frequency for the convex configuration by approximately 36%.

In figure 17, the vertical component of vorticity, ω_z , is shown at planes normal to the cylinder axis. Consistent with the wake topology and the sectional forces, the shear layers are interacting in the top two planes, while the wake becomes more symmetric as the junction of the curved with the straight cylinder part is approached.

Similar to the previous cases, the variation of pressure and velocity components along this body is shown in figure 18. The magnitude of the w velocity component at 0.3 diameters radially upstream of the stagnation face increases along the span and reaches a maximum of 20% of the free-stream magnitude at $s/D = 16$. This non-dimensional arclength corresponds to a section inclined at approximately 45.8° to the horizontal. Hence the maximum \bar{w} velocity component occurs at exactly the

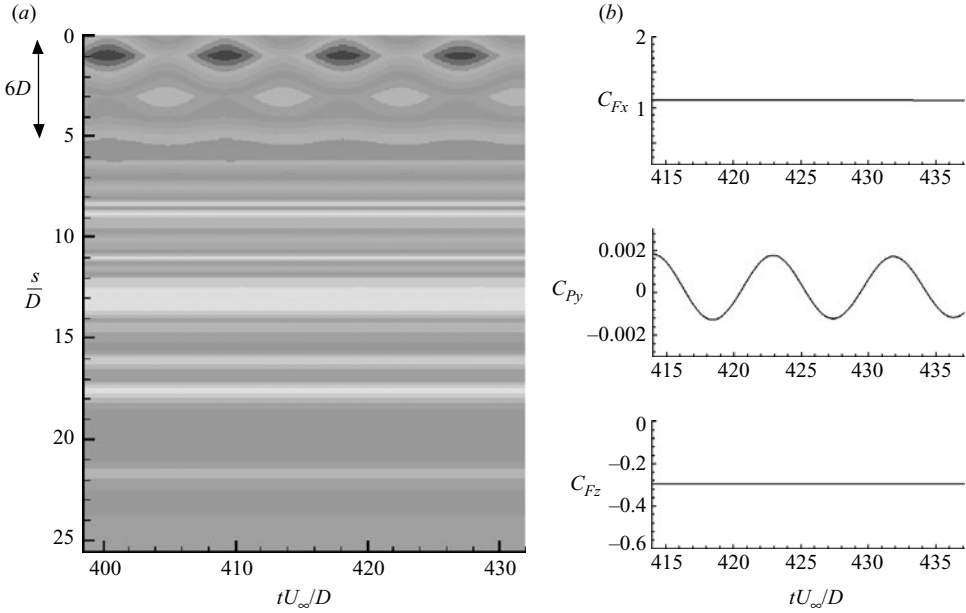


FIGURE 16. (a) Variation of sectional C_{Fy} for the concave configuration with a 6-diameter straight cylinder extension vertically, $Re = 100$; the isocountours range from -0.025 to $+0.025$. (b) Integrated force coefficients ($P = 6$): x is the direction of the drag, y is the horizontal component of the transverse force and z is the vertical one.

same location for this configuration as for the convex and concave configuration. The vertical addition has not affected the distribution of the \bar{w} velocity component along the length of the curved part of the body. As in the case without extension, the magnitude of the \bar{w} velocity component increases with downstream distance and at a line located 1.5 diameters radially downstream of the body it reaches a maximum of 84% of the free-stream value at a non-dimensional arclength of $s/D = 12.5$ (see figure 23a). We also note the presence of a \bar{w} velocity component of the order of 20% of the free-stream value at the rear of the cylinder in the vertical extension part.

5.3. Basic geometry, $Re = 500$

The wake topology for this case is shown in figure 19 and demonstrates how the experiments carried out in the towing tank are in good agreement with the numerical flow visualizations. The vortex-shedding features are again absent, even though a slight unsteadiness is present at the top as a consequence of the force fluctuations in the y -direction, illustrated in figure 20. The magnitude of the force coefficient in the x -direction is smaller by 19% compared to the convex case at the same Reynolds number. These plots show that the forces are not completely steady as in the $Re = 100$ case: fluctuations are evident in the integrated C_{Fy} and can be attributed to the top part of the concave configuration. More specifically, figure 20(a) depicts the sectional distribution of forces, at $s/D = 2$ the oscillatory component of sectional C_{Fy} has the largest amplitude, equal to 0.25. By $s/D = 4$, the amplitude of these fluctuations has dropped to less than a half, equal to 0.10, and subsequently, the amplitudes of the oscillatory components decreasing with increasing s/D . Finally, at $s/D = 7.5$ the forces are steady.

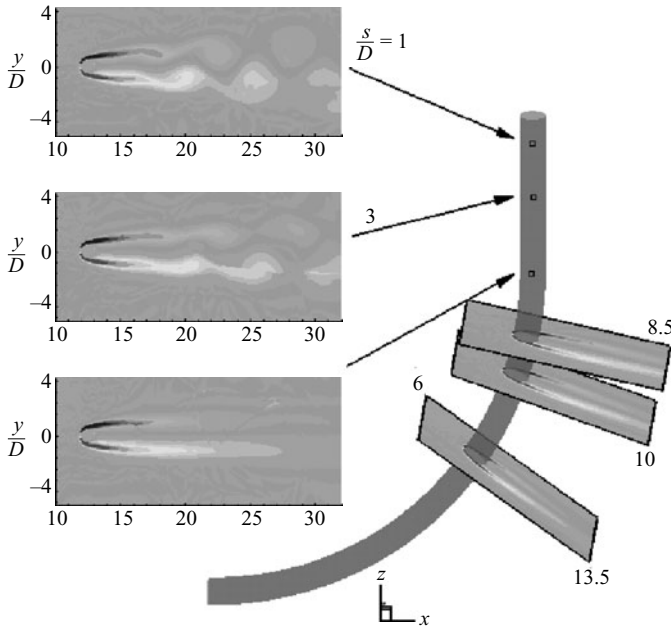


FIGURE 17. Spanwise vorticity contours for the concave configuration with a straight cylinder extension of 6 diameters at $Re = 100$, $tU_\infty/d = 414$, C_{Fy} maximum.

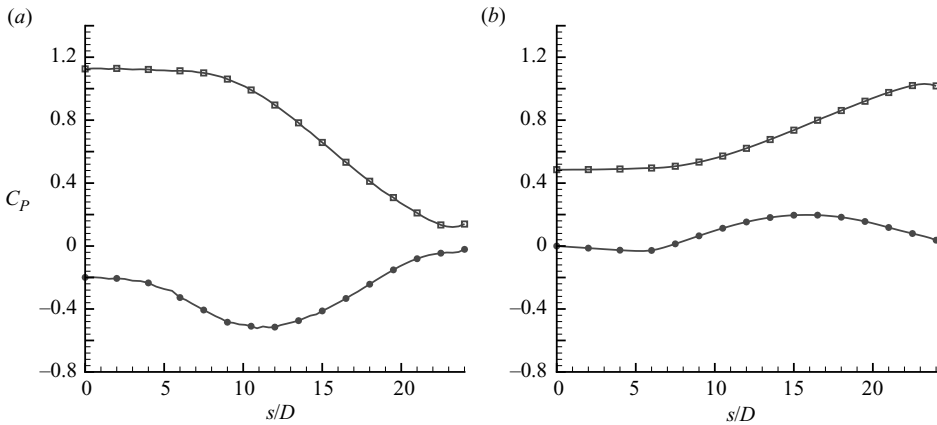


FIGURE 18. Variation of time-averaged pressure and velocity along the span of the concave configuration with a 6-diameter straight cylinder extension, $Re = 100$: (a) \bullet , base pressure and \blacksquare , stagnation pressure, (b) \blacksquare , u and \bullet , w velocity components extracted 0.3 diameters upstream of the curved cylinder.

Figure 21 shows the variation of pressure and velocity components along the span of the concave configuration at a Reynolds number of 500. Figure 21(b) shows that the magnitude of the \bar{w} velocity component 0.3 diameters radially upstream of the curved cylinder reaches a maximum of 18% of the free-stream value at a section inclined at 47.7° to the horizontal. Comparing this plot with figure 12, we see that the maximum value of the \bar{w} component occurs at a slightly lower section.

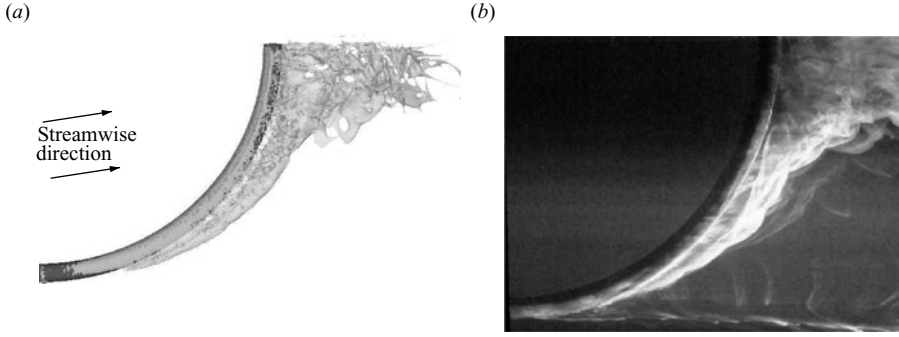


FIGURE 19. (a) Wake topology for the concave bend at $Re = 500$, $\lambda_2 = -0.4$, $tU_\infty/D \approx 616$ (C_{Fy} maximum). (b) Towing-tank flow visualization for the concave body, $Re = 500$.

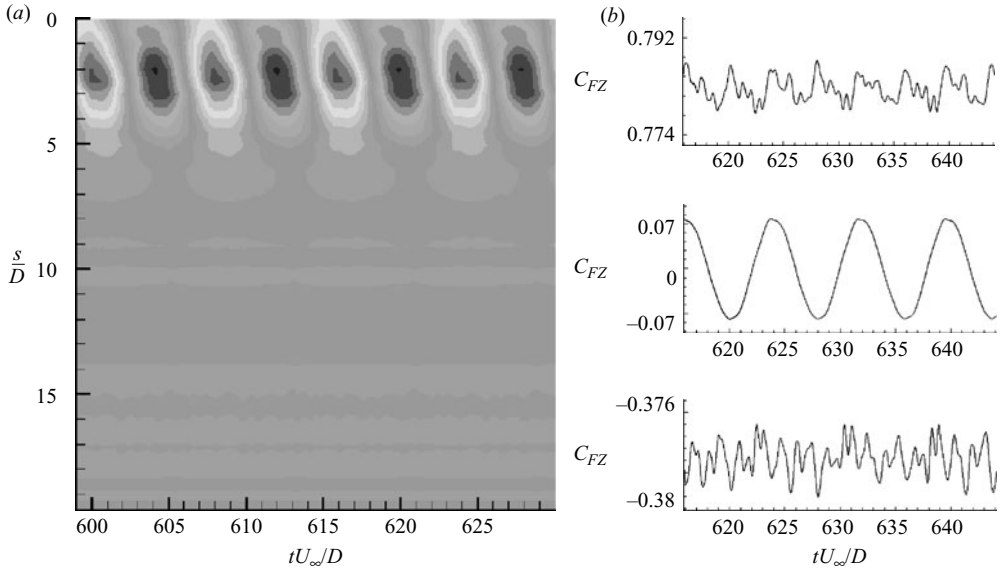


FIGURE 20. (a) Variation of sectional C_{Fy} along the length of the concave configuration, $Re = 500$; the isocontours range from -0.25 to $+0.25$. (b) Integrated force coefficients ($P = 6$).

5.4. Influence of the symmetry plane, $Re = 500$

The sectional forces for this geometry and the integrated force coefficients for this case are shown in figures 22(a) and 22(b), respectively. At this Reynolds number, it is not the straight cylinder extension on the top of the curved body that contributes the most to the unsteadiness, but rather the sections further down the span. This can be attributed to the high magnitude of the vertical velocity component in the wake of the body: as shown in figure 23, at $Re = 500$, the vertical velocity \bar{w} reaches the same order of magnitude as the free-stream velocity ($\bar{w} = 1.1U_\infty$ at a section inclined at 30.9° , on a line 0.6 diameters downstream in the radial direction). This peak is notably higher than the same case at $Re = 100$, where $w = 0.77U_\infty$. Furthermore, we observe that the largest fluctuations in the sectional forces are detected for $s/D \approx 6 - 8$ and not at the top part as expected and in contrast with the equivalent geometry at a lower Reynolds number. Note from figure 20(a) that for the flow past the concave configuration at $Re = 500$ without a vertical extension, the oscillatory component

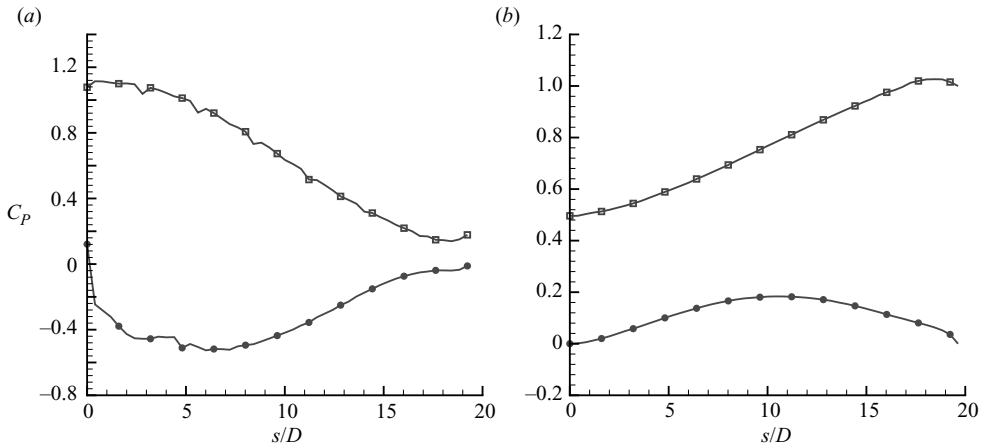


FIGURE 21. Variation of time-averaged pressure and velocity along the span of the concave configuration, $Re = 500$. (a) \bullet , Base pressure and \blacksquare , stagnation pressure, (b) \blacksquare , \bar{u} and \bullet , \bar{w} velocity components extracted 0.3 diameters upstream of the curved cylinder.

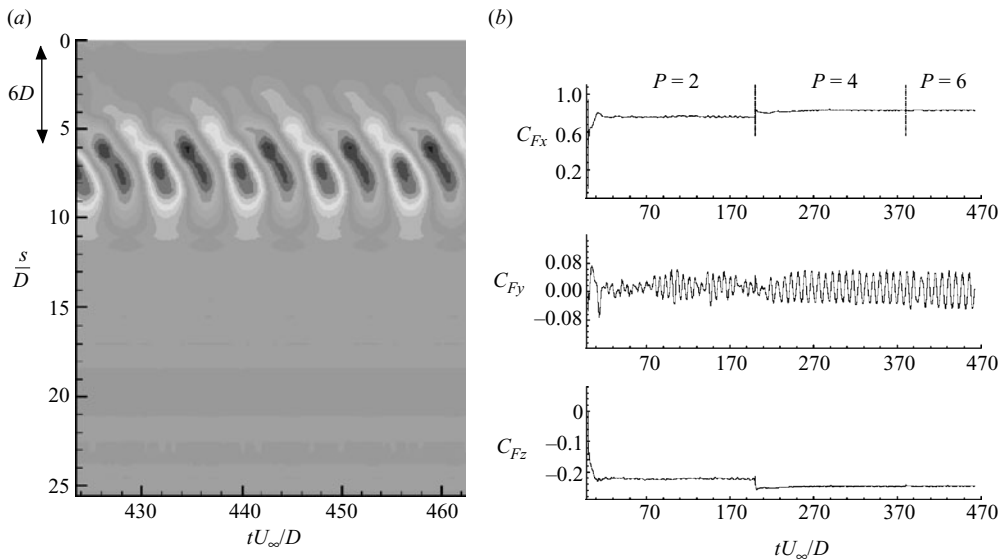


FIGURE 22. (a) Variation of sectional C_{Fy} for the concave bend with a vertical extension, $Re = 500$; the isocontours range from -0.32 to $+0.32$. (b) Integrated force coefficients for the flow past the concave bend with a vertical addition, $Re = 500$.

of sectional C_{Fy} has the largest amplitude at a similar value of $s/D \approx 2$. Since this case does not have the vertical extension, this corresponds to a sectional location of $s/D \approx 8$ in the modified geometry. However, there is a much larger amplitude of fluctuations in this case, having an amplitude of 0.3 compared to 0.06 without the boundary extension.

The variation of pressure and velocity components, extracted 0.3 diameters radially upstream of the curved cylinder, is similar to the case without the extension and so is not displayed here. Once again, the magnitude of the \bar{w} velocity component at 0.3 diameters radially upstream of the stagnation face increases along the span until

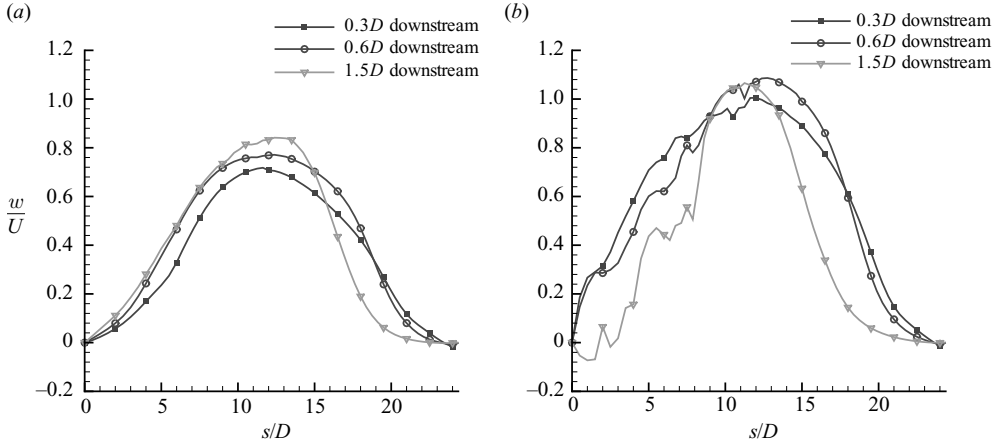


FIGURE 23. Variation of the time-averaged \bar{w} velocity component downstream of the concave configuration with a 6-diameter straight cylinder extension: (a) $Re = 100$, (b) $Re = 500$.

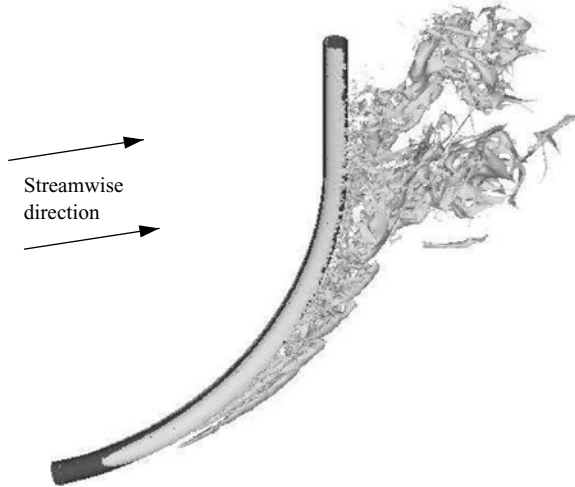


FIGURE 24. Wake topology for the concave configuration with a 6-diameter straight cylinder extension vertically at $Re = 500$, $\lambda_2 = -0.6$, $tU_\infty/d \approx 432$, C_{Fy} maximum.

reaching a maximum of 20% of the free-stream value at a section inclined at 45.8° from the horizontal ($s/D = 16$).

Finally, figure 24 shows the wake topology through λ_2 isocontours: the flow just below the top of the cylinder exhibits greater streamwise momentum deficit than at the sections below, where the streamwise vortex structures are convected downstream. The towing-tank flow visualization for this case is in good qualitative agreement with the numerical results.

6. Discussion: concave configuration

6.1. Steady-wake features: concave configuration

We have observed from §5 that there are significant differences in the flow features of the concave configuration as compared to the convex case. Most, strikingly, at

both $Re = 100$ and 500 , the majority of the wake has become steady. The completely different wake features observed for the convex and concave cases can be associated to the strong velocity component parallel to the stagnation face. Both the convex and concave configurations generate a vertical w velocity component and axially aligned flow (see figures 5*b* and 12*b*); however, the direction of the velocity depends on the orientation of the leading edge. In the concave geometry, this flow is directed towards the top of the domain where the stagnation face flow becomes increasingly normal to the free-stream velocity direction. From a purely geometrical point of view we would have expected the top of the concave configuration to be the region most susceptible to periodic vortex shedding. However, instead, the stagnation flow, which has ultimately to become aligned to the free stream, leads to a wider wake as compared to the width of the separated shear layer at the bottom of the concave geometry. This type of wake variation can equivalently be considered as generating streamwise component of vorticity. The wider wake and the equivalent generation of streamwise vorticity tend then to make the shear layer less susceptible to rolling up in a von Kármán street.

Qualitatively similar wake behaviour was observed in the computational work of Darekar & Sherwin (2001) and the experimental work of Bearman & Owen (1998*a, b*). These papers considered the flow past circular and square cylinders whose spanwise centreline was deformed sinusoidally making a ‘wavy cylinder’. In this work a leading-edge cross-flow was also observed where the flow was displaced along the span from the most upstream wavy section to the most downstream part of the spanwise waviness or the ‘geometrical minimum’. The flow which was displaced into the most downstream section subsequently leads to a wider separated shear layer as compared to the most upstream cross-sections and this wake variation can also be considered as generating streamwise vorticity within the separating shear layers around the cylinder.

In the current model, we might consider the ring segment we have studied as a quarter of a wavelength of a highly wavy geometry aligned vertically to the flow. In the wavy square cylinder work of Darekar & Sherwin (2001), the sinusoidal wavelength of the wavy geometry was denoted by λ and the peak-to-peak wave height was denoted by W . The wavy cylinders considered in this work were up to a maximum of $W/\lambda = 0.25$ and $\lambda/D = 11$; the analogous parameters for the concave geometry would be $W/\lambda = 0.5$ and $\lambda/D = 50$. Although these values lie outside the parameter space investigated by Darekar & Sherwin, some interesting comparisons can be drawn. As mentioned, the widest part of the wake along the span of the wavy cylinder was found to be at the geometrical minimum. The equivalent to the ‘geometrical minimum’ in the concave configuration is at the top computational plane, $z = 0$, which exhibits the widest wake (figure 10). We further note that the wavy wake regime III(A) of Darekar & Sherwin (2001) at $Re = 100$ had a symmetric wake with respect to the cylinder centreline and longer shear layers, similar to the symmetric topology of the concave configuration at the same Reynolds number. This regime was also the most stable of the cases considered, where the largest drag reduction and suppression of the vortex street were observed. When a time-independent state is reached, the lift force is zero and the drag has reduced by about 16% when compared to the drag on an undeformed cylinder. This value is close to the reduction achieved in the concave configuration (12%) at the same Reynolds number. Similarly, the increase in base pressure for the concave configuration is consistent with the lower drag as compared to the flow past the convex geometry. In the wavy square cylinders, the separation point was fixed by the geometry, in contrast to the circular cylinders studied in this

work. Nevertheless, the upstream cross-flow induced by the geometry, steady-wake features and the subsequent drag reduction suggest that the stabilization mechanism may be similar.

We finally note that the increase in Reynolds number from 100 to 500 has not altered the majority of the steady features of the lower-Reynolds-number flow near the body. The flow structures observed are similar with the exception of the occurrence of weak shedding at the top of the cylinder.

6.2. Weak shedding and the influence of the symmetry boundary condition

Since our motivation in considering the concave and convex deformed cylinder was as part of a longer cylinder, which would not be highly deformed, we are motivated to ask what influence the artificial symmetry boundary condition imposed on the computational domain plays in the vortex suppression. We therefore considered in §§ 5.2 and 5.4 a modified geometry to demonstrate the extent to which the steady features found for the flow past the concave configuration would persist, even with the top of the body reconnected to a straight cylinder addition. We had anticipated that flow past this configuration would resume the shedding close to the vertical extension and also allow us to assess the effect of the axial flow on the classical mechanism of vortex formation in the wake of a nominally two-dimensional body.

The results demonstrate that rather than the straight part of the cylinder influencing the curved region and destabilizing the steady wake found for the concave configuration, the curved part influences the vertical extension and weakens the two-dimensional shedding expected for a straight circular cylinder at $Re = 100$. Since the axial flow along the stagnation face is directed towards the vertical extension, this result might be anticipated.

However, at $Re = 100$, even at the top of the straight extension where periodic sectional fluctuations are observed, the vortex cores do not appear to form fully and remain, at least in the near wake, where they are partly attached to the developing shear layers lower down the body. The root-mean-square value of the lift coefficient from the mean, C'_{Fy} , at $s/D = 1$ is 5×10^{-3} and reduces to 2.4×10^{-3} at $s/D = 3$ and finally a steady state is reached at the junction of the vertical extension with the curved part ($s/D = 6$). In comparison to what we would expect for flow past a straight cylinder of $C'_{Lrms} = O(0.5)$, a relatively weak form of shedding develops, consistent with the wake topology depicted in figure 15.

The attenuation of vortex shedding can also be associated with the increased length of the formation region and the consequent decrease of the Strouhal number. At $Re = 100$, the frequency of the horizontal component of the transverse force shows a reduction of approximately 36% when compared to the value for the convex configuration (which was 0.1761 when $P = 8$). For a straight cylinder at the same Reynolds number, the $St - Re$ plot based on the experimental data obtained by Williamson (1989) indicates a Strouhal number of approximately 0.164, which is lower than that found for the convex case, but considerably higher than the value for the concave configuration.

When increasing the Reynolds number from $Re = 100$ to $Re = 500$, rather than observing a strong two-dimensional vortex shedding past the vertical extension, we observe that shedding primarily occurs at the junction between the deformed and straight cylinders (figure 22a). Although not presented in the results section at $Re = 500$, the magnitude of the streamwise vorticity generated in the near-body shear layers was larger than at $Re = 100$. Potentially more significantly, the w velocity component in the wake also grew to a similar magnitude as the free stream, U_∞ . Bearman

(1967) investigated the effects of base bleed on the flow past a two-dimensional model with a blunt trailing edge and found that the regular vortex street pattern broke down with sufficiently large bleed quantities. Similarly, we found that the shedding at the top of the vertical extension is suppressed by the axially aligned flow at the rear of the cylinder becoming parallel to the free-stream direction (owing to the upper numerical boundary condition) and acting as a base bleed type mechanism.

We have therefore observed that the concave configuration can partially suppress the vortex shedding in a straight cylinder attached to the curved one. At the junction between these two geometries, the straight extension has also influenced the overall wake dynamics, as indicated by the fact that at the plane $z=0$ there is a much narrower wake than at the same spanwise location for the concave configuration without vertical addition (see figure 10). If the vertical extension were sufficiently long, we would expect two-dimensional shedding to be re-established eventually. Further, a longer straight extension would potentially allow the flux of axially aligned fluid from the curved cylinder to be re-aligned into the free-stream direction in a more benign manner where vortex suppression may not take place. Nevertheless, the current results indicate that the dynamics in this region are likely to be highly three-dimensional and not amenable to sectional/two-dimensional interpretation.

7. Conclusions

In this paper, two configurations of uniform external flow past a deformed cylinder whose centreline followed a quarter segment of a ring were investigated at $Re = 100$ and $Re = 500$. The two geometries were fixed so that the plane of curvature of the deformed cylinder was aligned to the free-stream direction with one end parallel to the flow and the other normal to it. Finally, in one configuration, the flow was directed onto the outside of the deformed cylinder (convex configuration), whilst in the other case, the flow approached the inside of the bend (concave configuration). We have demonstrated how these geometries lead to very different highly three-dimensional flow patterns which are dependent on the orientation of the stagnation face and cross-validated the simulations with flow visualizations at comparable conditions.

Our investigations have demonstrated the following features in the two configurations considered.

(i) In both the concave and convex configurations, there was a significant component of flow in front of, and aligned to, the stagnation face with a magnitude of approximately 30% of the free-stream flow. In the concave configuration, a similar type of flow was also observed immediately behind the cylinder.

(ii) In the convex configuration, vortex shedding was observed to be driven primarily by shedding arising at the top of the cylinder, which is where the geometry is normal to the free stream. The shedding had a single frequency all along the cylinder, which is in contrast to what would be predicted by a sectional argument where each two-dimensional section is analysed independently by considering the normal local flow. A sectional argument would predict a variation in shedding frequency. A rudimentary alternative sectional modelling has been suggested, based on the top vortex-shedding frequency and on the phase offset related to the time required for the free stream to reach the stagnation face.

(iii) In the concave configuration, vortex shedding was completely suppressed at $Re = 100$, although a milder form of shedding at a Strouhal frequency significantly lower than that for the classical two-dimensional shedding was observed at $Re = 500$ at the top of the geometry. The suppression of vortex shedding consequently leads to a

reduction in total drag. The mechanism behind the vortex suppression was attributed to the stagnation face flow and the associated production of streamwise vorticity in the developing shear layers of the cylinder. This type of vortex suppression has previously been observed in flow past wavy cylinders (Darekar & Sherwin 2001): in both cases, this suppression mechanism is also associated with a large variation of wake width along the span.

(iv) To examine the effect of the artificial top computational boundary conditions in the concave geometry, a vertical extension, 6-diameter long, was considered. This modification did not destabilize the steady wake features of the deformed geometry; on the contrary, the curved geometry weakened the expected two-dimensional shedding behind the region normally aligned to the free stream. The mechanism behind the disruption of the two-dimensional shedding was attributed to a significant (around 30% of the free stream) axially aligned component of flow drawn behind the cylinder into the straight part of the configuration and acting in a similar manner to a base bleed mechanism as this flow is re-orientated into the free stream. A natural extension to this work would be to perform a gradual increase of the length of the vertical addition to investigate the threshold where the top vertical cylinder begins to shed in a classical two-dimensional manner at $Re = 100$. However, there is a significant increase in computational expense in undertaking this extension and so this was not possible within this study.

The authors would like to acknowledge computing facilities at the Imperial College Parallel Computing Centre, the EPSRC Turbulence Consortium and facilities within the Department of Aeronautics. We would also like to acknowledge funding support for the researchers from EPSRC. Finally, we would like to thank Dr Christine Hogan and Dr John Owen for their help in obtaining the flow visualizations.

REFERENCES

- BARKLEY, D., TUCKERMAN, L. S. & GOLUBITSKY, M. 2000 Bifurcation theory for three-dimensional flow in the wake of a circular cylinder. *Phys. Rev. E* **61**, 5247–5252.
- BEARMAN, P. W. 1967 The effect of base bleed on the flow behind a two-dimensional model with a blunt trailing edge. *Aeronaut. Q.* **18**, 207–224.
- BEARMAN, P. W. & OWEN, J. C. 1998a Special brief note: reduction of bluff-body drag and suppression of vortex shedding by the introduction of wavy separation lines. *J. Fluids Struct.* **12**, 123–130.
- BEARMAN, P. W. & OWEN, J. C. 1998b Suppressing vortex shedding from bluff bodies by the introduction of wavy separation lines. In *1998 Conference on Bluff Body Wakes and Vortex-Induced Vibration, ASME Fluids Engineering Division (Annual Summer Meeting), Washington, DC*.
- BEARMAN, P. W. & TAKAMOTO, M. 1988 Vortex shedding behind rings and discs. *Fluid Dyn. Res.* **3**, 214–218.
- BLACKBURN, H. M., MARQUES, F. & LOPEZ, J. M. 2005 Symmetry breaking of two-dimensional time-periodic wakes. *J. Fluid Mech.* **522**, 395–411.
- DAREKAR, R. M. & SHERWIN, S. J. 2001 Flow past a square-section cylinder with a wavy stagnation face. *J. Fluid Mech.* **426**, 263–295.
- GASTER, M. 1969 Vortex shedding from slender cones at low Reynolds numbers. *J. Fluid Mech.* **38**, 565–576.
- GERICH, D. & ECKELMANN, H. 1982 Influence of end plates and free ends on the shedding plates of circular cylinders. *J. Fluid Mech.* **122**, 109–121.
- JEONG, J. & HUSSAIN, F. 1995 On the identification of a vortex. *J. Fluid Mech.* **285**, 69–94.
- KARNIADAKIS, G. E. & SHERWIN, S. J. 1999 *Spectral/hp Element Methods for CFD*. Oxford University Press.

- KARNIADAKIS, G. E., ISRAELI, M. & ORSZAG, S. A. 1991 High-order splitting methods for the incompressible Navier–Stokes equations. *J. Comput. Phys.* **97**, 414–443.
- LEAR, C. J. 2003 Controlling the break-up distance of aircraft trailing vortices. PhD thesis, University of London.
- LEWEKE, T. & PROVANSAL, M. 1995 The flow behind rings–bluff-body wakes without end effects. *J. Fluid Mech.* **288**, 265–310.
- MASKELL, E. C. 1963 A theory of blockage effect on bluff-bodies and stalled wings in a closed wind tunnel. *ARC R&M 3400*.
- MENEGHINI, J. R., SALTARA, F., DE ANDRADE FERGONESI, R., YAMAMOTO, C. T., CASAPRIMA, E. & FERRARI, J. A. JR 2004 Numerical simulations of viv on long flexible cylinders immersed in complex flow fields. *Eur. J. Fluid Mech. B/Fluids* **23**, 51–63.
- MILIOU, A., SHERWIN, S. J. & GRAHAM, J. M. R. 2003 Fluid dynamic loading on curved riser pipes. *Trans. ASME J. Offshore Mech. Arctic Engng* **125**, 176–182.
- OWEN, J. C. 2001 Passive control of vortex shedding in the wakes of bluff bodies. PhD thesis, University of London.
- PEIRÓ, J. & SAYMA, A. I. 1995 A 3-d unstructured multigrid Navier–Stokes solver. In *Numerical Methods for Fluid Dynamics, V* (ed. K. W. Morton & M. J. Baines). Oxford University Press.
- PEIRÓ, J., PERAIRE, J. & MORGAN, K. 1994 *Felisa Manual*. Department of Aeronautics, Imperial College of Science, Technology and Medicine.
- PERAIRE, J., PEIRÓ, J. & MORGAN, K. 1993 Multigrid solution of the 3-d compressible Euler equations on unstructured tetrahedral grids. *Intl J. Numer. Meth. Engng* **36**, 1029–1044.
- SHERWIN, S. J. & KARNIADAKIS, G. E. 1996 Tetrahedral *hp* finite elements: algorithms and flow solutions. *J. Comput. Phys.* **124**, 14–45.
- SHERWIN, S. J. & PEIRÓ, J. 2002 Mesh generation in curvilinear domains using high-order elements. *Intl J. Numer. Meth. Engng* **53**, 207–223.
- SLAOUTI, A. & GERRARD, J. H. 1981 An experimental investigation of the end effects on the wake of a circular cylinder towed through water at low Reynolds numbers. *J. Fluid Mech.* **112**, 297–314.
- TAKAMOTO, M. & IZUMI, K. 1981 Experimental observation of stable arrangement of vortex rings. *Phys. Fluids* **24**, 1582–1583.
- WILLDEN, R. H. J. & GRAHAM, J. M. R. 2004 Multi-modal vortex-induced vibrations of a vertical riser pipe subject to a uniform current profile. *Eur. J. Fluid Mech. B/Fluids* **23**, 209–218.
- WILLIAMSON, C. H. K. 1988 The existence of two stages in the transition to three dimensionality of a cylinder wake. *Phys. Fluids* **31**, 3165–3168.
- WILLIAMSON, C. H. K. 1989 Oblique and parallel modes of vortex shedding in the wake of a circular cylinder at low Reynolds numbers. *J. Fluid Mech.* **206**, 579–627.